Proceedings of HT2007
2007 ASME-JSME Thermal Engineering Summer Heat Transfer Conference
July 8-12, 2007, Vancouver, British Columbia, CANADA

HT2007-32475

AN INTERFACIAL TRACKING METHOD FOR ULTRASHORT PULSE LASER MELTING AND RESOLIDIFICATION OF A THIN METAL FILM

Yuwen Zhang and J. K. Chen
Department of Mechanical and Aerospace Engineering
University of Missouri-Columbia
Columbia, MO 65211, USA
Email: zhangyu@missouri.edu

ABSTRACT

An interfacial tracking method is developed to model rapid melting and resolidification of a free-standing metal film subject to an ultrashort laser pulse. The laser energy is deposited to the electrons near thin film surface, and subsequently diffused into deeper part of the electron gas and transferred to the lattice. The energy equations for the electron and lattice are coupled through an electron-lattice coupling factor. Melting and resolidification are modeled by considering the interfacial energy balance and nucleation dynamics. An iterative solution procedure is employed to determine the elevated melting temperature and depressed solidification temperature in the ultrafast phase-change process. The predicted surface lattice temperature, interfacial location, interfacial temperature, and interfacial velocity are compared with those obtained by an explicit enthalpy model. The effects of the electron thermal conductivity models, ballistic range, and laser fluence on the melting and resolidification are also investigated.

INTRODUCTION

Microscale heat transfer has drawn the attention of many researchers due to its importance in many advanced manufacturing and materials processing. The traditional phenomenological laws, such as Fourier's law of heat conduction, are challenged in the microscale regime because (1) the characteristic lengths of the various heat carriers are comparable to each other and to the characteristic length of the system considered, and/or (2) the characteristic times of the various heat carriers are comparable to the characteristic energy excitation time [1]. Thus, microscale heat transfer can be referred to as heat transfer occurring on both the micro-length and micro-time scales. Microscale heat transfer finds applications in thin film (micro- length scale) as well as ultra-short pulsed laser processing (micro- time scale).

Ultrafast laser material processing has received significant attention due to a growing need for the fabrication of miniaturized devices at micro- and nanoscales. When the laser pulse is reduced to a nanosecond (10^{-9} sec) or less, the heat flux of the laser beam can be as high as 10^{12} W/m^2. For femtosecond pulse lasers, the laser intensity can even be up to 10^{21} W/m^2. Compared to long pulsed laser processing, short-pulsed laser processing enables users to precisely control the size of the heat-affected zone, the heat rate, and the interfacial velocity. Griffith *et al.* [2] investigated femtosecond laser machining of steel and developed the femtosecond laser micro-fabrication capability in the microscale regime. Klein-Wiele *et al.* [3] introduced a new technology of laser processing via ablation for nano-fabrication of solid materials with femtosecond laser. Heat affected zone of metals ablated with femtosecond laser was investigated by Hirayama and Obara [4].

During laser-metal interaction, the laser energy is first deposited into electrons on the metal surface, where two competing processes occur [5]. One is ballistic motion of the excited electrons into deeper parts of the metal with velocity close to the Fermi velocity (~10^6 m/s). Another process is collision between the excited electrons and electrons around the Fermi level – an electron temperature is defined upon establishment of equilibrium among hot electrons. These hot electrons are then diffused into deeper part of the electron gas at a speed (<10^4 m/s) much lower than that of the ballistic motion. Meanwhile, the hot electrons are cooled by transferring their energy to the lattice through electron-phonon coupling. The nonequilibrium between electrons and lattice has been observed experimentally [6, 7] and can be described by the two-temperature model, which was originally proposed by

Anisimov *et al.* [8] and rigorously derived by Qiu and Tien [9] from the Boltzmann transport equation. The nonequilibrium electron and lattice temperature model can also be derived using the dual-phase-lag model by considering lagging behavior of different energy carrier [10, 11]. Jiang and Tsai extended the existing two-temperature model to high electron temperatures by using full-run quantum treatments [12]. Chen *et al.* proposed a semi-classical two-step heating model to investigate thermal transport in metals caused by ultrashort laser heating [13].

Most existing two-temperature models dealt with the case that lattice temperature is well below the melting point and only pure conduction is considered. Under higher laser fluence and/or short pulse, the lattice temperature can exceed the melting point and melting takes place. The liquid phase will be resolidified when the lattice is cooled by conducting heat away. Short-pulsed laser melting of thin film involves the following three steps [14]: (1) absorption of photon energy by free electrons, (2) energy transfer between the free electrons and the lattice, and (3) phase change of the lattice due to the propagation of energy. The rapid phase change phenomena induced by ultrashort pulse laser are controlled by nucleation dynamics at the interface, not by interfacial energy balance [15]. The solid-liquid interface can be heated well above the melting point during a rapid melting process, in which case the solid becomes superheated. Similarly, the solid-liquid interface can be cooled far below the melting point in the rapid solidification process, in which case the liquid becomes undercooled. Both superheated solid and undercooled liquid are thermodynamically metastable states. Once phase change is triggered in a superheated solid or undercooled liquid, the solid-liquid interface can move at an extremely high velocity (on the order of 10 to 10^3 m/s). When the laser fluence is sufficiently high [16] or when the laser pulse width is in the order of femtosecond [17], the liquid surface temperature may exceed the saturation temperature and vaporization may take place.

Many numerical models for melting and solidification of various Phase Change Materials (PCMs) have been developed. The numerical models can be divided into two groups [18]: *deforming grid schemes* (or strong numerical solutions) and *fixed grid schemes* (or weak numerical solutions). Deforming grid schemes transform solid and liquid phases into fixed regions by using a coordinate transformation technique. The governing equations and boundary conditions are complicated due to the transformation. However, the disadvantage of deforming grid schemes is that it requires significant amount of computational time. On the contrary, the fixed grid schemes use one set of governing equations for the whole computational domain including both liquid and solid phases, and solid-liquid interface is later determined from the temperature distribution. This simplicity makes the computation much faster than deforming grid schemes, while it still provides reasonably accurate results [19]. There are two main methods in the fixed grid schemes: the enthalpy method and the equivalent heat capacity method. The enthalpy method [20] can solve heat transfer in mushy zone but has difficulty with temperature oscillation, while the equivalent heat capacity method [21, 22] requires large enough temperature range in mushy zone to obtain converged solution. Cao and Faghri [23] combined the advantages of both enthalpy and equivalent heat capacity methods and proposed a Temperature Transforming Model (TTM) that could also account for natural convection.

The energy equation for electrons was solved using a semi-implicit Crank-Nicholson scheme, while the energy equation and phase change for lattices was solved using an explicit enthalpy model in Ref. [14, 17]. While explicit scheme is very easy to apply, a very small time step is required to ensure stability. Development of an implicit scheme for enthalpy model that can outperform explicit scheme is numerically challenging [18]. The temperature transforming model [23] and the enthalpy linearization model [24] are two very efficient models that can be easily discretized using implicit scheme. These two models assume phase change occurs in a range of temperature near melting point, which prevents inclusion of superheat in solid in melting stage and undercooling of liquid in the solidification stage. In this paper, a fixed grid interfacial tracking method is proposed to solve kinetics controlled rapid melting and resolidification during ultrashort pulse laser interaction with a free-standing metal film. Effects of electron thermal conductivity model, ballistic range, and laser fluence on the phase change processes are investigated.

NOMENCLATURE

B_e	Coefficient for electron heat capacity [J/m^3-K^2]
C	heat capacity, [J/m^3-K]
c_p	specific heat, [J/kg-K]
f	liquid fraction
G	electron-lattice coupling coefficient [W/m^3-K]
H_l	enthalpy of lattice per unit volume [J/m^3]
h_m	latent heat of fusion [J/kg]
J	heat source fluence (J/m^2)
k	thermal conductivity [W/m-K]
L	thickness of the metal film [m]
M	molar mass [kg/kmol]
R	reflectivity
R_g	gas constant [J/kg-K]
s	solid-liquid interfacial location [m]
S	intensity of the internal heat source [W/m^3]
t	time [s]
t_p	FWHM (Full Width at Half Maximum) pulse width [s]
T	temperature [K]
T_m	melting point [K]
$T_{l,I}$	lattice temperature at solid-liquid interface [K]
u_s	solid-liquid interfacial velocity [m/s]
V_0	interfacial velocity factor [m/s]
x	coordinate [m]

Greek Symbols

δ	optical penetration depth [m]
δ_b	ballistic range [m]
ρ	density [kg/m^3]

Subscripts

e	electron
i	initial
l	lattice
ℓ	liquid
s	solid

Physical Model

The physical model of the problem under consideration is shown in Fig. 1. A metal film with a thickness of L and an initial temperature of T_i is subjected to a temporal Gaussian laser pulse with a FWHM (Full Width at Half Maximum) pulse width of t_p and fluence of J (J/m^2) from the left surface (x = 0). The problem can be approximated to be one-dimensional because the radius of the laser beam is significantly larger than the metal film thickness. The energy equation of the free electrons is

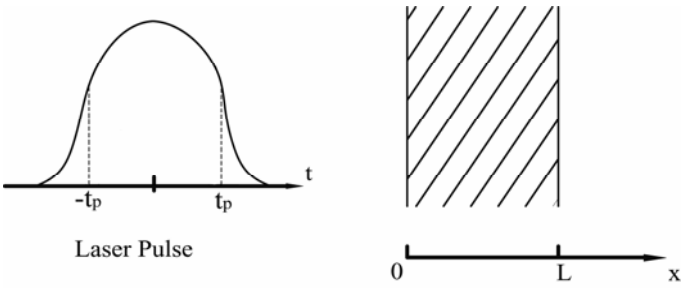

Fig. 1 Laser melting of thin film

$$C_e \frac{\partial T_e}{\partial t} = \frac{\partial}{\partial x}\left(k_e \frac{\partial T_e}{\partial x} \right) - G\left(T_e - T_l\right) + S \tag{1}$$

which is valid in the entire computational domain. The energy equation for the lattice is

$$C_l \frac{\partial T_l}{\partial t} = \frac{\partial}{\partial x}\left(k_l \frac{\partial T_l}{\partial x} \right) + G\left(T_e - T_l\right) \tag{2}$$

which is valid in both solid and liquid phases but not at the solid-liquid interface. The heat capacity of electron is proportional to the electron temperature, i.e.,

$$C_e = B_e T_e \tag{3}$$

The bulk thermal conductivity of metal measured at equilibrium, k_{eq}, is the sum of electron thermal conductivity, k_e, and the lattice thermal conductivity, k_l. Since the mechanism for heat conduction in metal is diffusion of free electron, k_e is usually dominate. For gold, k_e is 99% of k_{eq}, while k_l only contributes to 1% of k_{eq} [25]. At nonequilibrium condition, thermal conductivity of the electrons depends on the temperatures of both electrons and lattice [14], i.e.,

$$k_e = k_{eq}\left(\frac{T_e}{T_l}\right) \tag{4}$$

where $k_{eq}(T)$ is the thermal conductivity of the electron when the electrons and lattice are in thermal equilibrium. Equation (4) is valid when the electron temperature is much lower than the Fermi temperature, T_F, which is 6.42×10^4 K for gold. If the electron temperature is comparable to Fermi temperature, the electron temperature can be calculated by [26]

$$k_e = \chi \frac{(\vartheta_e^2 + 0.16)^{5/4}(\vartheta_e^2 + 0.44)\vartheta_e}{(\vartheta_e^2 + 0.092)^{1/2}(\vartheta_e^2 + \eta\vartheta_l)} \tag{5}$$

where $\vartheta_e = T_e / T_F$ and $\vartheta_l = T_l / T_F$. The two constants in eq. (5) are $\chi = 353$ W/m-K and $\eta = 0.16$ for gold. For high electron temperature, $\vartheta_e \gg 1$, eq. (5) results in the well-known dependence $k_e \sim T_e^{5/2}$ that is the characteristics of low-density plasma. On the other hand, eq. (5) will reduce to eq. (4) under low electron temperature limit, $\vartheta_e \ll 1$. The difference between the results obtained by using thermal conductivities will be discussed later. The electron-lattice coupling factor, G, for liquid is 20% higher than that of the solid, because electrons collide more frequently with liquid atoms than with the atoms in the solid crystals [14].

The source terms in eq. (1) can be described by the following equation:

$$S = 0.94\frac{1-R}{t_p \delta} J \exp\left(\frac{x}{\delta} - 2.77\left(\frac{t}{t_p}\right)^2 \right) \tag{6}$$

where R is reflectivity of the thin film, t_p is laser pulse duration (s), δ is the optical penetration depth (m), and J is laser pulse fluence (J/m^2). While eq. (6) is widely used in many existing works, Wellershoff *et al.* [27] and Hohlfeld *et al.* [5] suggested that the ballistic motion and diffusion of the hot electrons spread the absorbed laser energy into much greater depth of electrons, especially for the s/p-band metals. This hot electron bath should be initially localized within either the ballistic range (for s/p-band metals) or the optical penetration depth. Therefore, it is necessary to incorporate the effect of the ballistic motion and hot electron diffusion by adding the ballistic range, δ_b, to the optical penetration depth in eq. (6), i.e.,

$$S = 0.94\frac{1-R}{t_p(\delta + \delta_b)[1 - e^{-L/(\delta+\delta_b)}]} J \exp\left(\frac{x}{\delta + \delta_b} - 2.77\left(\frac{t}{t_p}\right)^2 \right) \tag{7}$$

where $[1 - e^{-L/(\delta+\delta_b)}]$ is to correct the film thickness effect. The effect of ballistic motion on the ultrafast melting and resolidification will be discussed later.

The lattice thermal conductivity, k_ℓ, is taken as 1% of the thermal conductivity of bulk metal, k_{eq}, since the mechanism of heat conduction in metal is mainly by electrons [14, 25], i.e.,

$$k_l = 0.01 k_{eq} \tag{8}$$

While many researchers suggested that the conduction term in eq. (2) be negligible [e.g., 9, 12], Chen and Beraun [28] showed that inclusion of lattice conduction resulted in more accurate thermal response than the models without lattice conduction. As will become evident later, large lattice temperature gradients in solid and liquid phases exist near the solid-liquid interface during ultrashort pulse laser induced melting and resolidification and therefore, lattice conduction is included in this work.

While the energy equation for electrons, eq. (1) is valid for both solid and liquid phases, the coupling factor for solid and liquid phases are different. For energy equation of lattice, eq. (2), is valid for both solid and liquid phase, but not at interface. The energy balance at the solid-liquid interface is [29]

$$k_{l,s}\frac{\partial T_{l,s}}{\partial x}-k_{l,\ell}\frac{\partial T_{l,\ell}}{\partial x}=\rho_\ell h_m u_s \qquad x=s(t) \tag{9}$$

where the additional interfacial velocity due to the density change during melting and solidification has been considered.

For the conventional melting process, the velocity of the solid-liquid interface is obtained by energy balance as specified by eq. (9). However, this is not the case for rapid melting/solidification processes, because the velocity of the interface is dominated by nucleation dynamics. For short-pulsed laser melting of gold, the velocity of the solid-liquid interface is described by [14]

$$u_s=V_0\left[1-\exp\left(-\frac{h_m}{R_g T_m}\frac{T_{l,I}-T_m}{T_{l,I}}\right)\right] \tag{10}$$

where V_0 is the maximum interface velocity, R_g is the gas constant for the metal, and $T_{l,I}$ is the interfacial temperature. The interfacial temperature, $T_{l,I}$, is higher than melting point, T_m, during melting and lower than melting point during solidification.

The time $t = 0$ is defined as the time when the peak of a laser pulse reaches the film surface. Therefore, the initial conditions of the problem are

$$T_e(x,-2t_p)=T_l(x,-2t_p)=T_i \tag{11}$$

The boundary conditions of the problem can be specified by assuming that the heat loss from the film surface can be neglected, i.e.,

$$\left.\frac{\partial T_e}{\partial x}\right|_{x=0}=\left.\frac{\partial T_e}{\partial x}\right|_{x=L}=\left.\frac{\partial T_l}{\partial x}\right|_{x=0}=\left.\frac{\partial T_l}{\partial x}\right|_{x=L}=0 \tag{12}$$

Numerical Solution and Interfacial Tracking

The computational domain (0, L) is discretized using non-uniform grid. The implicit finite difference equations are obtained by integrating eqs. (1) and (2) in each control volume and time step [30]. The electron temperature can be obtained by

$$a_{e,P}T_{e,P}=a_{e,W}T_{e,W}+a_{e,E}T_{e,E}+b_e \tag{13}$$

where $T_{e,P}$, $T_{e,W}$ and $T_{e,E}$ are, respectively, electron temperatures at grid P, W, and E at the current time step (see Fig. 2). The coefficients in eq. (13) are:

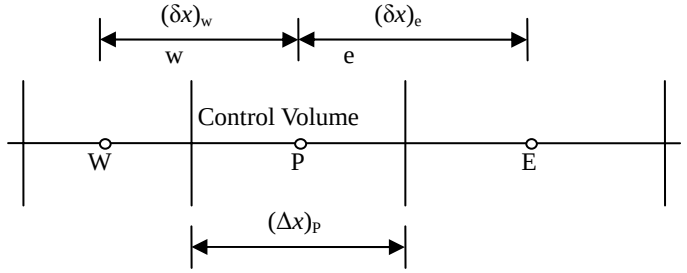

(a) Single phase control volume

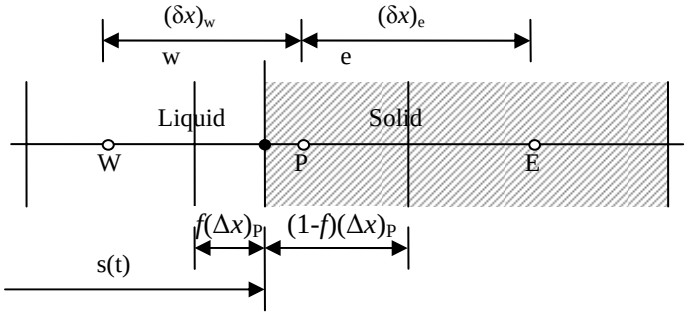

(b) Control volume with interface

Fig. 2 Grid system

$$a_{e,W}=\frac{k_{e,w}}{(\delta x)_w} \tag{14}$$

$$a_{e,E}=\frac{k_{e,e}}{(\delta x)_e} \tag{15}$$

$$b_e=a_{e,P}^0 T_{e,P}^0+(G_P T_{l,P}+S_P)(\Delta x)_P \tag{16}$$

$$a_{e,P}^0=\frac{C_{e,P}(\Delta x)_P}{\Delta t} \tag{17}$$

$$a_{e,P}=a_{e,P}^0+a_{e,W}+a_{e,E}+G_P(\Delta x)_P \tag{18}$$

where $k_{e,w}$ and $k_{e,e}$ are electron conductivity at the faces of control volume, e and w, and they are obtained by harmonic averaging the thermal conductivities at the two control volumes [30]. $T_{e,P}^0$ is electron temperature at grid point P for the previous time step, $T_{l,P}$ is lattice temperature at grid point P for the current time step, and S_P is intensity of the heat source at grid point P.

For a control volume that contains only one phase, the lattice temperature can be obtained by integrating eq. (2) in control volume P, i.e.,

$$a_{l,P}T_{l,P}=a_{l,W}T_{l,W}+a_{l,E}T_{l,E}+b_l \tag{19}$$

where $T_{l,P}$, $T_{l,W}$ and $T_{l,E}$ are, respectively, electron temperatures at grid P, W, and E at the current time. The coefficients in eq. (19) are:

$$a_{l,W}=\frac{k_{l,w}}{(\delta x)_w} \tag{20}$$

$$a_{l,E} = \frac{k_{l,e}}{(\delta x)_e} \tag{21}$$

$$b_l = a_{l,P}^{\ 0} T_{l,P}^{\ 0} + G_P T_{e,P} (\Delta x)_P \tag{22}$$

$$a_{l,P}^{\ 0} = \frac{C_{l,P} (\Delta x)_P}{\Delta t} \tag{23}$$

$$a_{l,P} = a_{l,P}^{\ 0} + a_{l,W} + a_{l,E} + G_P (\Delta x)_P \tag{24}$$

where the lattice conductivity at the faces of control volume are obtained by harmonic averaging the thermal conductivities at two control volumes, $T_{l,P}^{\ 0}$ is the lattice temperature at grid P for the previous time step.

Wang and Matthys [31] proposed an effective interface-tracking method by introducing an addition node at the interface, which divides the control volume that containing interface into two control volumes. This approach could accurately account for energy balance at the interface because the solid-liquid interface is always between two small control volumes. In this paper, an alternative approach that does not require dividing the control volume containing interface but can still accurately account for energy balance at the interface will be developed. For the control volume that contains solid-liquid interface, the lattice temperature, $T_{l,P}$, is numerically set as interfacial temperature, $T_{l,I}$, by letting

$$a_{l,P} = 10^{20} \quad \text{and} \quad b_l = T_{l,I} \times 10^{20} \tag{25}$$

in eq. (19). This treatment will yield accurate result when the solid-liquid interface is exactly at the grid point P. When the interfacial location is not at the grip point P [see Fig. 2(b)], a modified thermal conductivity, $\hat{k}_{l,w}$, at the face of control volume, w, is introduced by equating the actual heat flux across the face of control volume, w, based on the position and temperature of the solid-liquid interface, to the heat flux at face w based on the position and temperature of main grid point, P [32], i.e.,

$$\frac{k_{l,w}(T_{l,W} - T_{l,I})}{(\delta x)_w - (0.5 - f_P)(\Delta x)_P} = \frac{\hat{k}_{l,w}(T_{l,W} - T_{l,P})}{(\delta x)_w} \tag{26}$$

Considering $T_{l,P} = T_{l,I}$, eq. (26) becomes

$$\hat{k}_{l,w} = \frac{(\delta x)_w}{(\delta x)_w - (0.5 - f_P)(\Delta x)_P} k_{l,w} \tag{27}$$

Similarly, a modified thermal conductivity at face e of the control volume can be obtained as

$$\hat{k}_{l,e} = \frac{(\delta x)_e}{(\delta x)_e + (0.5 - f_P)(\Delta x)_P} k_{l,e} \tag{28}$$

The modified thermal conductivities defined by eqs. (27) and (28) are used to obtain the coefficients for grid points W and E, which allows the temperature at the main gird P to be used in the computation, regardless the location of interface within the control volume. To determine the interfacial location and the interfacial temperature, the energy balance at the interface, eq. (9), and the nucleation dynamics, eq. (10), must be employed. The energy equation for the control volume that contains solid-liquid interface can be written in the enthalpy form:

$$\frac{\partial H_l}{\partial t} = \frac{\partial}{\partial x}\left(k_l \frac{\partial T_l}{\partial x} \right) + G\left(T_e - T_l\right) \tag{29}$$

The volumetric enthalpy can be expressed as

$$H_l = \int_0^{T_{l,I}} C_{l,s}(T_l) dT_l + f \rho_\ell h_m \tag{30}$$

where the first term is enthalpy of solid phase at the interfacial temperature, and the second term is the latent heat due to partial melting. Substituting eq. (30) into eq. (29), one obtains

$$C_{l,s}(T_{l,I}) \frac{\partial T_{l,I}}{\partial t} + \rho_\ell h_m \frac{\partial f}{\partial t} = \frac{\partial}{\partial x}\left(k_l \frac{\partial T_l}{\partial x} \right) + G\left(T_e - T_l\right) \tag{31}$$

which is applicable in the control volume that contains solid-liquid interface. The liquid fraction, *f*, is related to the location of the solid-liquid interface by [see Fig. 2 (b)].

$$\frac{\partial f}{\partial t} = \frac{1}{(\Delta x)_P} \frac{ds}{dt} = \frac{u_s}{(\Delta x)_P} \tag{32}$$

Substituting eq. (32) into eq. (31) and integrating the resulting equation in the control volume that contains solid-liquid interface, the solid-liquid interfacial velocity can be obtained as

$$u_s = \frac{1}{\rho_\ell h_m}\left[\frac{k_{l,w}(T_{l,W} - T_{l,I})}{(\delta x)_w - (0.5 - f_P)(\Delta x)_P} - \frac{k_{l,e}(T_{l,I} - T_{l,E})}{(\delta x)_e + (0.5 - f_P)(\Delta x)_P} + G_P (T_{e,P} - T_{l,P})(\Delta x)_P - C_{l,s}(T_{l,I})(T_{l,I} - T_{l,I}^0)\frac{(\Delta x)_P}{\Delta t} \right] \tag{33}$$

where $T_{l,I}^0$ is the solid-liquid interfacial temperature at the previous time step. The third and fourth terms in the bracket at the right-hand side of eq. (33) represent the effects of electron-lattice interaction and change of the interfacial temperature on the solid-liquid interfacial temperature. Equations (33) can be rewritten in a more compact from by considering eqs. (27) and (28), i.e.,

$$u_s = \frac{1}{\rho_\ell h_m}\left[\frac{\hat{k}_{l,w}(T_{l,W} - T_{l,P})}{(\delta x)_w} - \frac{\hat{k}_{l,e}(T_{l,P} - T_{l,E})}{(\delta x)_e} + G_P (T_{e,P} - T_{l,P})(\Delta x)_P - C_{l,s}(T_{l,I})(T_{l,I} - T_{l,I}^0)\frac{(\Delta x)_P}{\Delta t} \right] \tag{34}$$

which will be used together with eq. (10) to determine the solid-liquid phase interfacial velocity and the temperature. The interfacial location is then determined using

$$s = s^0 + u_s \Delta t \tag{35}$$

and the liquid fraction in the control volume that contain interface is

$$f = \frac{s - x_P - (\Delta x)_P / 2}{(\Delta x)_P} \tag{36}$$

The numerical solution starts from time $t = -2t_p$, and the initial temperatures of electrons and lattice are given by eq. (11). Before onset of melting, the electron and lattice temperatures are obtained by solving eqs. (13) and (19) simultaneously. Once the lattice temperature at the first control

volume from the heated surface obtained from eq. (19) (without phase change accounted for) exceeds the melting point, the lattice temperature of the first control volume is setting at the melting point using eq. (25) and phase change will be modeled. Since rapid melting and resolidification are controlled by nucleation dynamics, the interfacial temperature, $T_{l,I}$, is unknown and it is related to the interfacial velocity by eq. (10). After melting is initiated, the following iterative procedure is employed to solve for the interfacial temperature and the interfacial location at each time step:

1. The solid-liquid interfacial temperature, $T_{l,I}$, is assumed and eq. (34) is used to determine the solid-liquid phase interfacial velocity. The location of interface is determined using eq. (35) and the liquid fraction in the first control volume is determined using eq. (36).
2. The interfacial velocity from the nucleation dynamics is obtained from eq. (10) and compared with the interfacial velocity obtained from eq. (34) in Step 1. If the interfacial velocity obtained from eq. (34) is higher than that from eq. (10), the interfacial temperature will be increased; otherwise, the interfacial temperature is decreased.
3. Equations (13) and (19) [$a_{l,P}$ and b_l at the control volume that contains interface are altered using eq. (25)] are solved simultaneously to obtain the electron and lattice temperature distributions.
4. Steps 1 to 3 are repeated until the difference between the interfacial velocities obtained from eqs. (33) and (10) is less than 10^{-6} m/s.

Results and Discussions

Picosecond laser melting and resolidification of a free-standing pure gold film is simulated. In order to compare the results obtained by the present interfacial tracking method and those obtained by explicit enthalpy method in Ref. [14], the thermophysical properties of the gold in the present study, are exactly the same as those used in Ref. [14]. The thermophysical

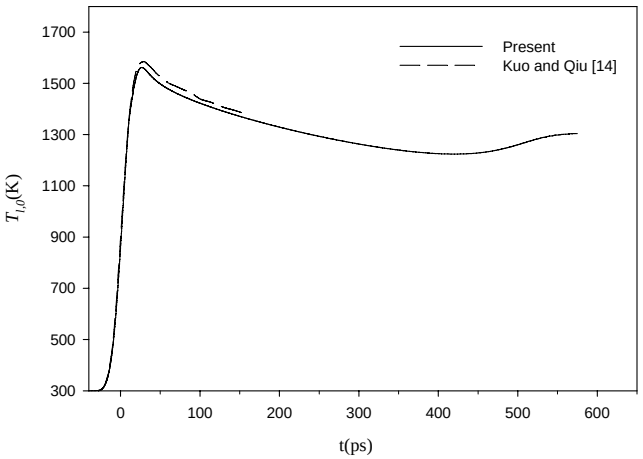

(a) Surface lattice temperature

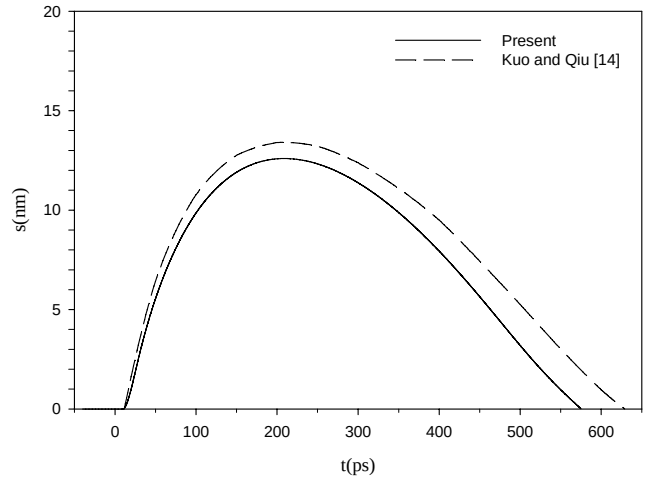

(b) Interfacial location

Fig. 3 Comparison of surface lattice temperatures and interfacial locations

Table 1 Thermophysical properties of gold [14]

Properties	Solid (*s*)	Liquid (*l*)
Coefficient for electron heat capacity, B_e(J/m^3-K)	70	
Electron-lattice coupling factor, G (W/m^3-K)	2.6×10^{16}	3.1×10^{16}
Density, ρ (kg/m^3)	19.30×10^3	17.28×10^3
Specific heat, c_p (J/kg-K) [a]	$105.1+0.2914T_l-8.713\times10^{-4}T_l^2+1.187\times10^{-6}T_l^3-7.051\times10^{-10}T_l^4+1.538\times10^{-13}T_l^5$	163.205
Thermal conductivity at equilibrium, k_{eq} (W/m-K) [a]	$320.973-0.0111T_l-2.747\times10^{-5}T_l^2-4.048\times10^{-9}T_l^3$	$37.72+0.0711T_l-1.721\times10^{-5}T_l^2+1.064\times10^{-9}T_l^3$
Reflectivity, *R*	0.6	
Optical penetration depth, δ (nm)	20.6	
Melting point, T_m (K)	1336	
Latent heat of fusion, h_m (J/kg)	6.373×10^4	
Limit velocity, V_0 (m/s)	1300	
Gas constant for gold, R_g (J/kg-K)	42.21	

[a] Correlations were obtained by curve-fitting data in Ref. [14].

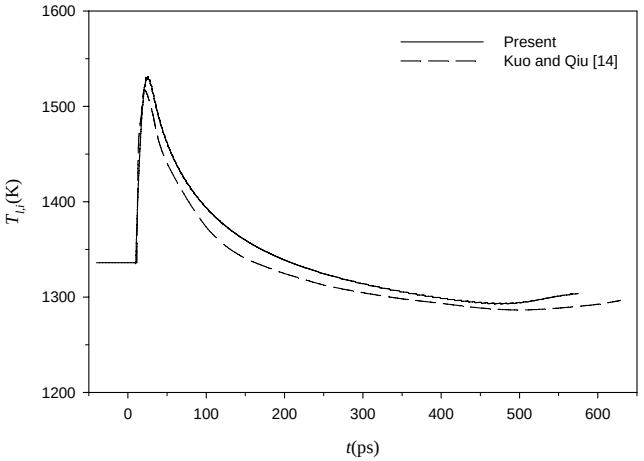

(a) Interfacial temperature

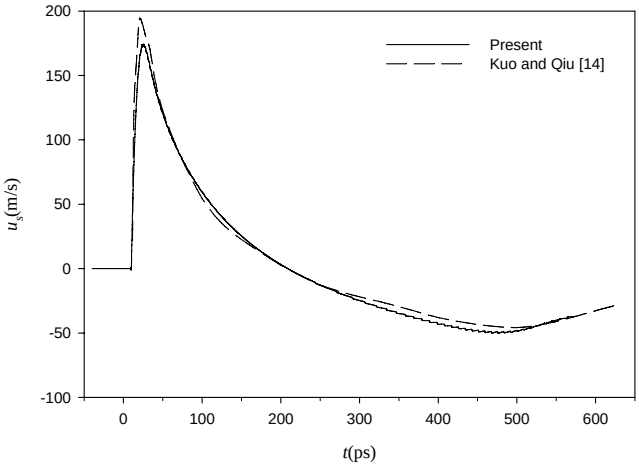

(b) Interfacial velocity

Fig. 4 Comparison of interfacial temperatures and velocities

properties of the gold listed in Table 1 are for solid below melting point and liquid above melting point only. The properties for the superheated solid and undercooled liquid are taken as those at the melting point because lack of properties for these nonequilibrium states.

Figure 3 shows comparison of the surface lattice temperature and interfacial location for a 1000-nm gold film under irradiation of a laser pulse with fluence of $J = 0.3$ J/cm^2 and a pulse width of $t_p = 20$ ps. Under the assumption that the electron temperature is much lower than the Fermi temperature and neglecting the effect of ballistic motion, the electron thermal conductivity was calculated from eq. (4) and the source term in eq. (1) was obtained from eq. (6). The grid number is 2502 and the time step is $\Delta t = 0.05$ ps. The peak surface lattice temperature is 1562 K and occurs at $t = 27$ ps, while the maximum melting depth is 12.59 nm and occurs at $t = 209$ ps. The peak temperature and the maximum melting depth obtained in the present paper are 1.4% and 6% lower than those obtained by Kuo and Qiu [14]. The duration of phase change in the present paper is 9% shorter than that obtained by Kuo and Qiu [14].

The interfacial temperature and velocity during the picosecond laser pulse and gold film interaction are shown in Fig. 4. Strong superheating in the melting stage and undercooling in the solidification stage can be observed in Fig. 4(a), although the degrees of superheating and undercooling in the present paper are slightly lower than that in Ref. [14]. The peak interfacial velocity in the present paper is lower than that in Ref. [14], which is consistent with the result in Fig. 3(b). The interfacial velocity reached to its peak at very early stage of phase change ($t = 23.5$ ps), and the phase change continues until $t = 575$ ps. Since interfacial velocity decreases in most part of phase change process ($23.5 \text{ ps} < t < 575 \text{ ps}$), the melting depth obtained by the present implicit scheme is smaller than that obtained by explicit scheme.

Figure 5 shows comparison between the lattice temperatures obtained by using the present model and those obtained by Kuo and Qiu [14]. Strong superheating of solid in the melting stage ($t = 100$ ps) and undercooling of the liquid phase in the resolidification stage ($t = 400$ ps) can be successfully predicted using the proposed interfacial tracking model. The slops of temperature curves near the interface obtained by the present paper are slightly lower than those obtained by Kuo and Qiu's [14] explicit enthalpy model, which is consistent with results shown in Figs. 3 and 4.

Numerical simulation is then performed using the electron thermal conductivity obtained from eq. (5) while all parameters are the same as those in Figs. 3 and 4. Comparison of the surface lattice temperature and the interfacial location obtained by using different thermal conductivities is shown in Fig. 6.

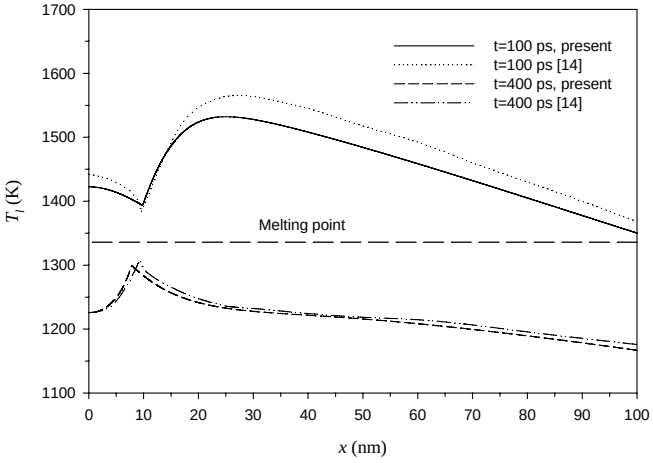

Fig. 5 Comparison of lattice temperature distributions

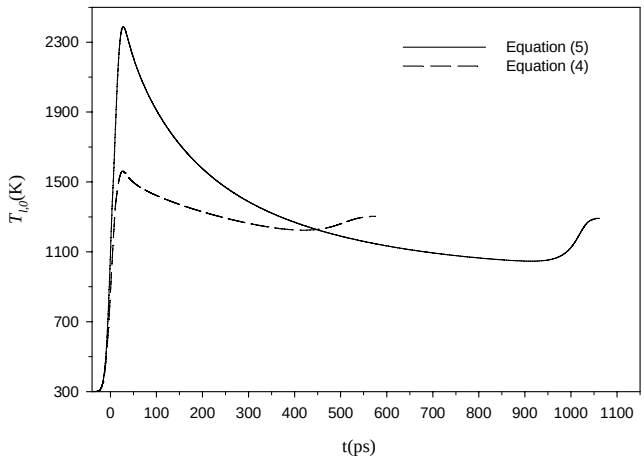

(a) Surface lattice temperature

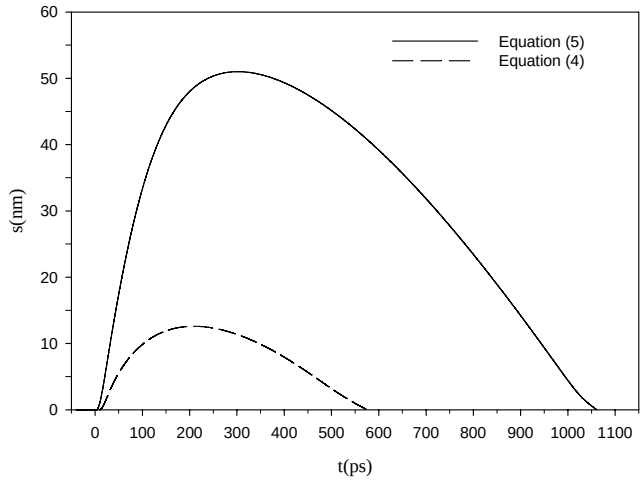

(b) Interfacial location

Fig. 6 Effect of electron thermal conductivities on the surface lattice temperatures and the interfacial locations

The peak surface lattice temperature obtained using eq. (5) is 2388 K occurring at $t = 28$ ps, while the maximum melting depth is 60 nm occurring at $t = 302$ ps. They are 53% and 377% higher than those obtained using eq. (4). The duration of phase change obtained using eq. (5) is 88% longer than that obtained using eq. (4). Comparison of the interfacial temperature and velocity obtained using different thermal conductivities are shown in Fig. 7. The maximum interfacial temperature in the melting stage obtained using eq. (5) is 2115 K, which is much higher than 1531 K obtained using eq. (4). The interfacial velocity obtained using eq. (5) peaks at 443 m/s as oppose to 174 m/s obtained using eq. (4). The results presented in Figs. 6 and 7 indicated that different model of electron thermal conductivity have significant effects on the results of ultrashort pulse laser interaction with metal film. The electron and temperature distributions at $t = 15$ ps obtained using eq. (5) are shown in Fig. 8 (a), and the corresponding electron thermal conductivity is shown in Fig. 8(b) as the solid line. The thermal conductivity using eq. (4) with temperatures in Fig. 8(a) is also plotted in Fig. 8(b) for comparison. When both electron and lattice temperatures are low, the thermal conductivity obtained from eq. (4) agreed with that obtained from eq. (5) very well. At higher electron and lattice temperature, however, the thermal conductivity obtained from eq. (4) is several times higher than that obtained from eq. (5). The differences between the results obtained using different thermal conductivities can be explained by the strong deviation of thermal conductivity models as shown in Fig. 8(b).

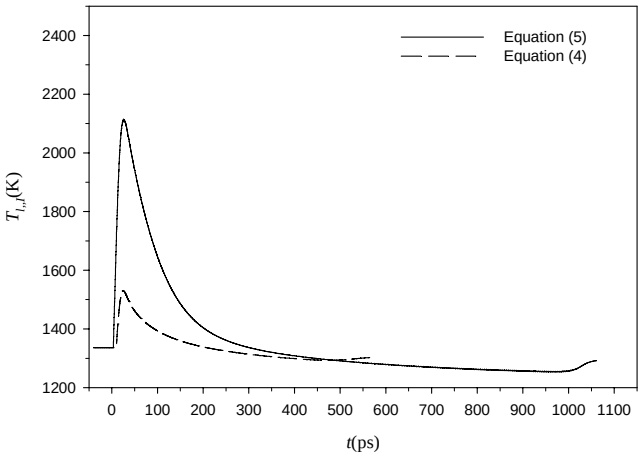

(a) Interfacial temperature

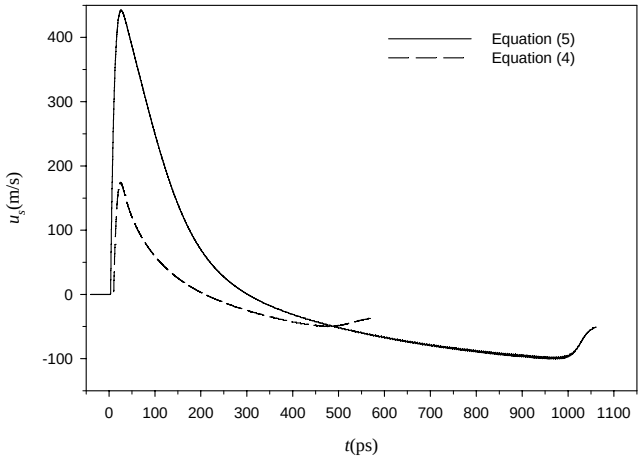

(b) Interfacial velocity

Fig. 7 Effect of electron thermal conductivities on the interfacial temperatures and velocities

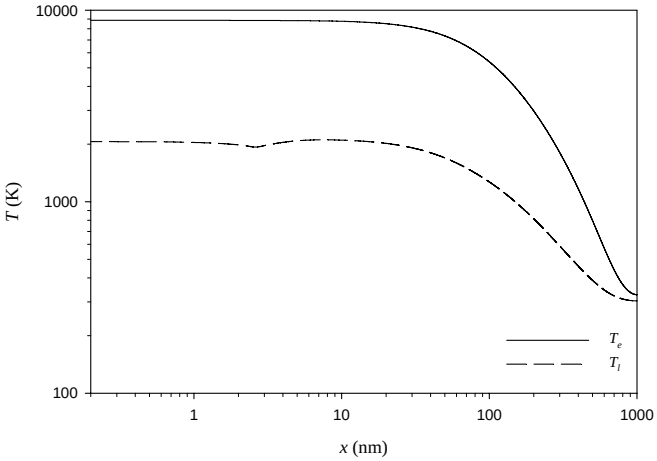

(a) Electron and lattice temperatures

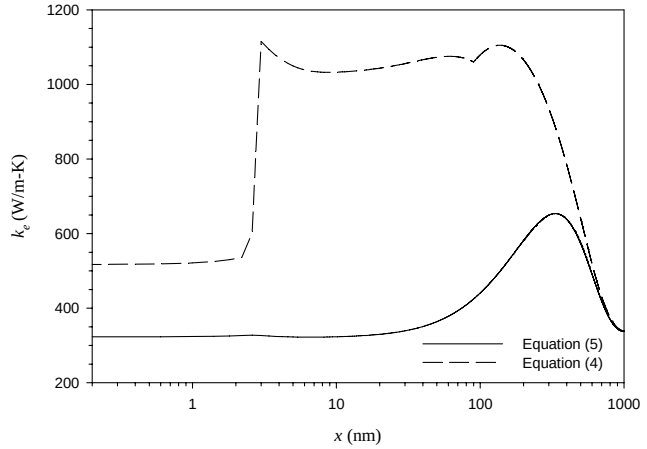

(b) Electron thermal conductivity

Fig. 8 Temperature and electron thermal conductivity distributions ($t = 15$ ps)

To investigate the effects of electron ballistic motion on the ultrashort laser melting and resolidification of metal film, simulation is carried out using the internal heat source defined in eq. (7). The ballistic motion range of the electrons is $\delta_b = 105$ nm as recommended in Ref. [27]. Comparison of the surface lattice temperatures and the interfacial locations obtained by using different heat sources is shown in Fig. 9. The peak surface lattice temperature obtained using eq. (7) is 1518 K occurring at $t = 27.5$ ps, while the maximum melting depth is 10.28 nm occurring at $t = 199$ ps. They are respectively 36% and 83% lower than those obtained with $\delta_b = 0$. The duration of phase change obtained using eq. (7) is 52% shorter than that obtained with $\delta_b = 0$. Figure 10 shows comparison of the interfacial temperature and velocity obtained using the different heat sources. The maximum interfacial temperature in the melting stage is reduced from 2115 K to 1499 K when ballistic motion of electrons is considered. The peak interfacial velocity is decreased from 443 m/s to 151 m/s due to the effect of ballistic motion. Figure 11 shows the effects of ballistic range on the electron and lattice temperature distributions. It can be seen that both electron and lattice temperatures in the region near the irradiated surface are lower when ballistic range is considered. This is attributed to the fact that the laser energy penetrates to deeper parts of the metal film when the effect of ballistic range is taken into account. The magnitudes of the results with the electron thermal conductivity from eq. (5) *and* the heat source from eq. (7) are comparable with those obtained using the simple electron conductivity model, eq. (4), and the heat source without ballistic range, eq. (6).

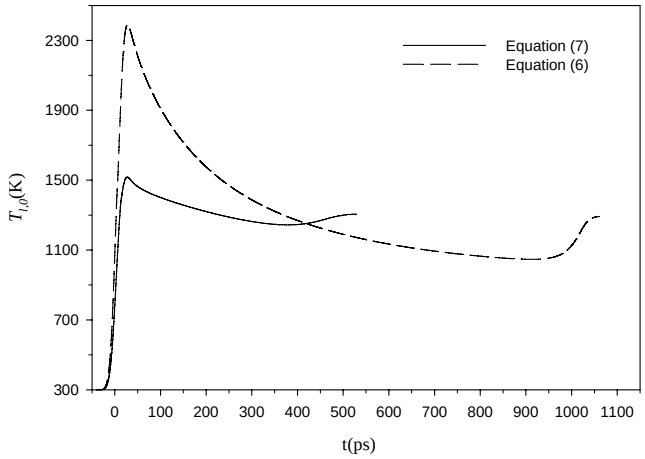

(a) Surface lattice temperature

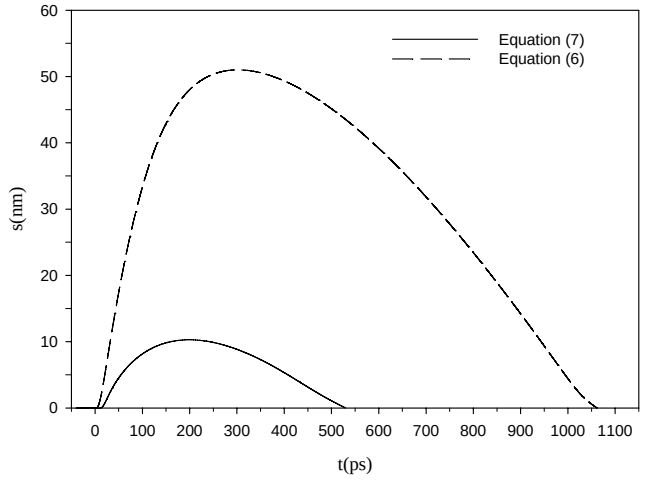

(b) Interfacial location

Fig. 9 Effect of ballistic range on the surface lattice temperatures and the interfacial locations

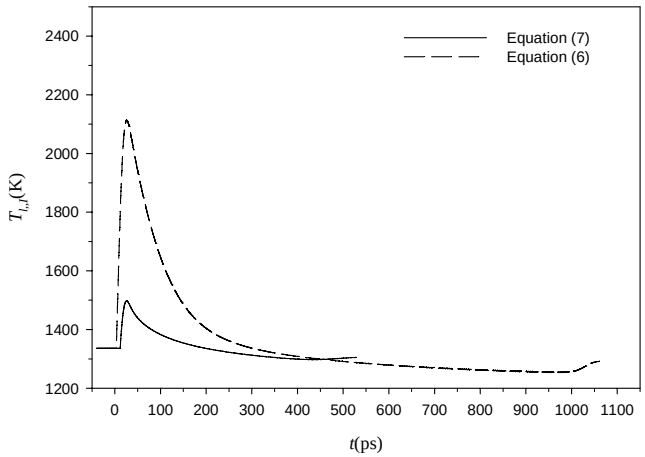

(a) Interfacial temperature

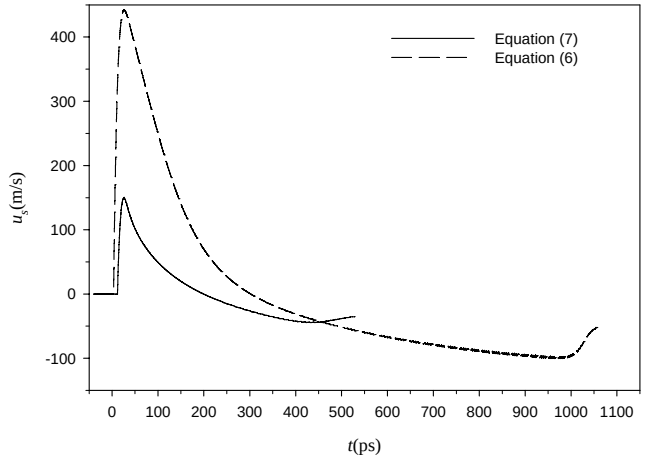

(b) Interfacial velocity

Fig. 10 Effect of ballistic range on the interfacial temperatures and velocities

Figure 12 shows the surface lattice temperatures and the interfacial locations at different laser fluence while the laser pulse width is kept at $t_p = 20$ ps . It can be seen that the surface lattice temperature increases significantly with increasing laser fluence. The time at which peak temperature occurs is slightly delayed with increasing laser fluence. The maximum melting depth is increased by 7.2 times when the laser fluence is increased from 0.3 J/cm^2 to 0.45 J/cm^2. The peak time at which maximum melting depth is reached significantly delays with increasing laser fluence. The duration of phase change is doubled when the laser fluence is increased from 0.3 J/cm^2 to 0.45 J/cm^2. Effects of laser fluence on the interfacial temperature and velocity are shown in Fig. 13. While the peak interfacial temperature during melting stage increases significantly – from 1499 K for $J = 0.3$ J/cm^2 to 2216 K for $J = 0.45$ J/cm^2 – with increasing laser fluence, the minimum interfacial temperature during the solidification stage is almost unaffected by the laser fluence. Similarly, the peak interfacial velocity is increased from 151 m/s for $J = 0.3$ J/cm^2 to 403 m/s for $J = 0.45$ J/cm^2, while the affect of laser fluence on the interfacial velocity during the solidification stage is insignificant.

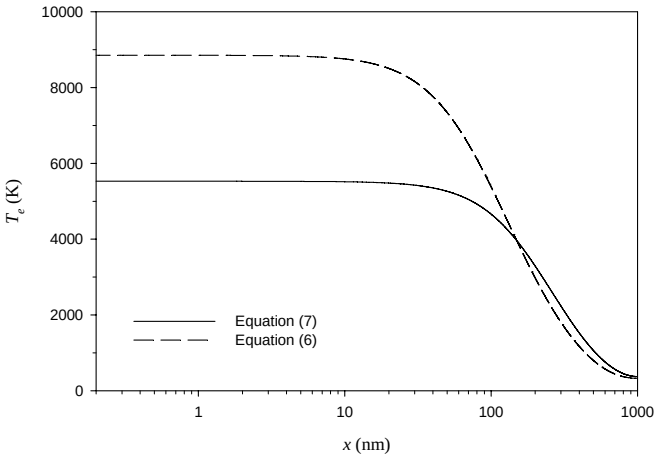

(a) Electron temperatures

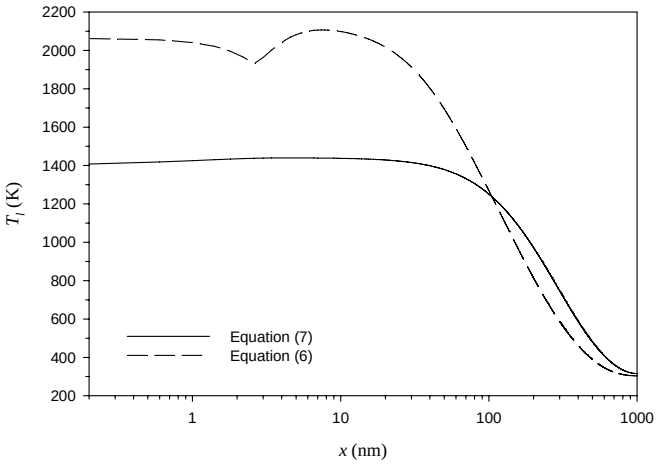

(b) Lattice temperature

Fig. 11 Effect of ballistic range on the electron and lattice temperature distributions ($t = 15$ ps)

Conclusions

An interfacial tracking method is developed to model ultrashort laser melting and resolidification of the metal film. The interfacial velocity and temperature were obtained by considering interfacial energy balance and nucleation dynamics. For the case with a simple electron thermal conductivity model, eq. (4), and without the electron ballistic motion, the results agreed with the existing results in the literature. When the more sophisticated electron thermal conductivity model, eq. (5), is employed, the interfacial

velocity and temperature were significantly increased due to the strong deviation between the two thermal conductivity models at high temperatures. Consideration of the ballistic range of electron motion results in penetration of laser energy into deeper parts of the metal film and thus lowers interfacial velocity and temperature. The maximum melting depth, peak interfacial temperature and velocity during the melting stage significantly increase with increasing laser fluence.

Acknowledgement

Support for this work by the University of Missouri System Research Board and the College of Engineering at University of Missouri-Columbia is gratefully acknowledged.

References

[1] Wang, G. X., Prasad, V., 2000, "Microscale Heat and Mass Transfer and Non-equilibrium Phase Change in Rapid Solidification," *Materials Science and Engineering*, **A292**, pp. 142-148.

[2] Griffith, M. L., Ensz, M. T., and Reckaway D. E., 2003, "Femtosecond Laser Machining of Steel," *Proceedings of SPIE*, **4977**, pp. 118-122.

[3] Klein-Wiele, J., Bekesi J., Ihlemann, J., and Simon, P., 2003, "Nanofabrication of Solid Materials with Ultraviolet Femtosecond Pulses," *Proceedings of SPIE*, Vol. 5399, pp. 139-46.

[4] Hirayama, Y., and Obara M., 2003, "Heat Affected Zone of Metals Ablated with Femtosecond Laser Pulses," *Proceedings of SPIE*, Vol. 4977, pp. 417-425.

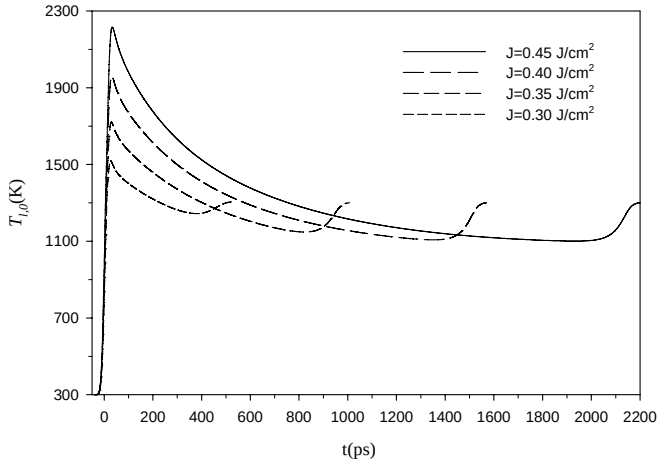

(a) Surface lattice temperature

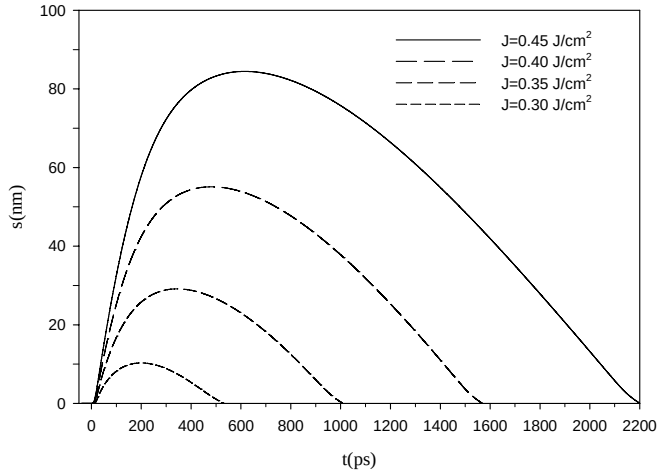

(b) Interfacial location

Fig. 12 Effect of laser fluence on the surface lattice temperatures and the interfacial locations (t_p = 20 ps)

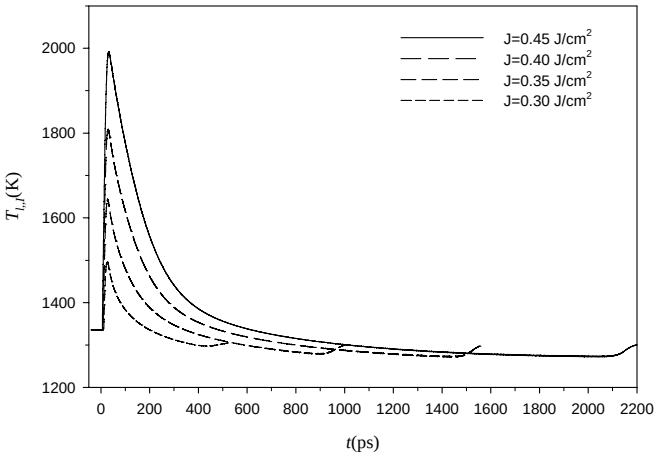

(a) Interfacial temperature

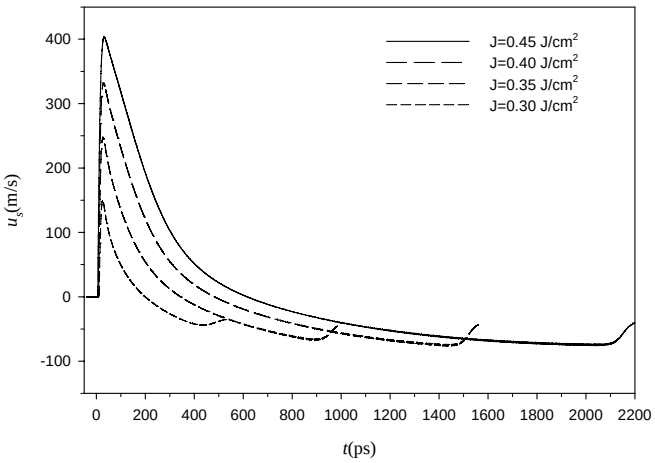

(b) Interfacial velocity

Fig. 13 Effect of laser fluence on the interfacial temperatures and velocities (t_p = 20 ps)

[5] Hohlfeld, J., Wellershoff, S. S., Gudde, J., Conrad, U., Jahnke, V., and Matthias, E., 2000, "Electron and Lattice Dynamics Following Optical Excitation of Metals," *Chemical Physics*, **251**, pp. 237-258.
[6] Eesley, G. L., 1986, "Generation of Non-equilibrium Electron and Lattice Temperatures in Copper by Picosecond Laser Pulses," *Physical Review* B, **33**, pp. 2144-2155.
[7] Elsayed-Ali, H. E., Norris, T. B., Pessot, M. A., and Mourou, G. A., 1987, "Time-Resolved Observation of Electron-Phonon Relaxation in Copper," *Physical Review Letters*, **58**, pp. 1212-1215.
[8] Anisimov, S. I., Kapeliovich, B. L., Perel'man, T. L., 1974, "Electron Emission from Metal Surface Exposed to Ultrashort Laser Pulses," Sov. Phys. JETP, **39**, pp. 375-377.
[9] Qiu, T. Q., and Tien, C. L., 1993, "Heat Transfer Mechanisms During Short-Pulse Laser Heating of Metals," *Journal of Heat Transfer*, **115**, pp. 835-837.
[10] Tzou, D. Y., *Macro- to Microscale Heat Transfer*, Taylor and Francis, Washington, DC, 1997.
[11] Tzou, D. Y., "Computational Techniques for Microscale Heat Transfer," in Minkowycz, W. J., Sparrow, E. M., and Murthy, J. Y., Eds., *Handbook of Numerical Heat Transfer*, 2nd ed., John Wiley & Sons, Hoboken, NJ, 2006.
[12] Jiang, L., and Tsai, H. L., 2005, "Improved Two-Temperature Model and Its Application in Ultrashort Laser Heating of Metal Films," ASME, *J. Heat Transfer*, **127**, pp. 1167-1173.
[13] Chen, J. K., Beraun, J. E., Tzou, D. Y., 2006, "A Semiclassical Two-Temperature Model for Ultrasfast Laser Heating," *Int. J. Heat and Mass Transfer*, **49**, pp. 307-316.
[14] Kuo, L. S., and Qiu, T., 1996, "Microscale Energy Transfer During Picosecond Laser Melting of Metal Films," ASME *National Heat Transfer Conference*, Vol. 1, pp. 149-157.
[15] Von Der Linde, D., Fabricius, N., Danielzik, B., and Bonkhofer, T., 1987, "Solid Phase Superheating During Picoseond Laser Melting," *Mat. Res. Symp. Proc.*, **74**, pp. 103-108.
[16] Shi, Y., Zhang, Y., and Konrad, C., "Solid-Liquid and Liquid-Vapor Phase Change Induced by a Nanosecond Laser in Selective Laser Sintering," *Nanoscale and Microscale Thermophysical Engineering*, 2006 (submitted).
[17] Chowdhury, I. H., and Xu X., 2003, "Heat Transfer in Femtosecond Laser Processing of Metal," *Numerical Heat Transfer*, Part A, **44**, pp. 219-232.
[18] Voller, V. R., 1997, "An Overview of Numerical Methods for Solving Phase Change Problems," in W. J. Minkowycz and E. M. Sparrow (Eds.)," *Advances in Numerical Heat Transfer*, Vol. 1, Taylor & Francis, Basingstoke.
[19] Sasaguchi, K., Ishihara, A. and Zhang, H., 1996, "Numerical Study on Utilization of Melting of Phase Change Material for Cooling of a Heated Surface at a Constant Rate," *Numerical Heat Transfer*, Part A, **29**, 19-31.
[20] Binet, B. and Lacroix, M., 2000, "Melting from Heat Sources Flush Mounted on a Conducting Vertical Wall," *Int. J. Num. Meth. Heat and Fluid Flow*, **10**, 286-306.
[21] Morgan, K., 1981, "A Numerical Analysis of Freezing and Melting with Convection," *Comp. Meth. App. Eng*., **28**, pp. 275-284.
[22] Hsiao, J. S., 1984, "An Efficient Algorithm for Finite Difference Analysis of Heat Transfer with Melting and Solidification," *ASME paper* No. 84-WA/HT-42.
[23] Cao, Y., and Faghri, A., 1990, "A Numerical Analysis of Phase Change Problem including Natural Convection," ASME *J. Heat Transfer*, **112**, 812-815.
[24] Swaminathan, C. R., and Voller, V. R., 1993, "On the Enthalpy Method," *Int. J. Heat Fluid Flow*, **3**, pp. 233-234.
[25] Klemens, P. G., and Williams, R. K., 1986, "Thermal Conductivity of Metals and Alloys," *Int. Metals Review*, 31, pp. 197-215.
[26] Anisimov, S. I., and Rethfeld, B., 1997, "On the Theory of Ultrashort Laser Pulse Interaction with a Metal," *Proceedings of SPIE*, **3093**, pp. 192-202.
[27] Wellershoff, S., Hohlfeld, J., Güdde, J., Matthias, E., 1999, "The Role of Electron-Phonon Coupling in Femtosecond Laser Damage of Metals," *Appl. Phys. A: Mater. Sci. Process*. **69**(Suppl.), pp. 99–107.
[28] Chen, J. K., and Beraun, J. E., 2001, "Numerical Study of Ultrashort Laser Pulse Interactions with Metal Films," *Numerical Heat Transfer A: Applications*, **40**, pp. 1-20.
[29] Faghri, A., and Zhang, Y., 2006, *Transport Phenomena in Multiphase Systems*, Elsevier, Burlington, MA.
[30] Patankar, S. V., 1980, *Numerical Heat Transfer and Fluid Flow*, McGraw-Hill, New York.
[31] Wang, G. X., and Matthys, E.F., 1992, "Numerical Modeling of Phase Change and Heat Transfer during Rapid Solidification Processes: Use of Control Volume Integral with Element Subdivision," *Int. J. Heat Mass Transfer*, **35**, pp. 141-153.
[32] Olsson, E. D., and Bergman, T. L., 1990, "Reduction of Numerical Fluctuations in Fixed Grid Solidification Simulations," AIAA/ASME Thermophysics and Heat Transfer Conference, Seattle, WA, June 18-20, ASME HTD-Vol. 130, pp. 130-140.

